A&A 471, 765–773 (2007)
DOI: 10.1051/0004-6361:20077649

Astronomy & Astrophysics

The dust distribution in edge-on galaxies

Radiative transfer fits of V and K'-band images[⋆,⋆⋆]

S. Bianchi

INAF – Istituto di Radioastronomia, Sezione di Firenze, Largo Enrico Fermi 5, 50125 Firenze, Italy
e-mail: `sbianchi@arcetri.astro.it`

Received 15 April 2007 / Accepted 3 May 2007

ABSTRACT

Aims. I have analyzed a sample of seven nearby edge-on galaxies observed in the V and K'-bands, in order to infer the properties of the dust distribution.

Methods. A radiative transfer model, including scattering, was used to decompose each image into a stellar disk, a bulge, and a dust disk. The parameters describing the distributions were obtained through standard χ^2 minimization techniques.

Results. The dust disks fitted to the V-band images are consistent with previous work in the literature: the radial scalelength of dust is larger than for stars ($h_\mathrm{d}/h_\mathrm{s} \sim 1.5$); the dust disk has a smaller vertical scalelength than the stellar ($z_\mathrm{d}/z_\mathrm{s} \sim 1/3$); the dust disk is almost transparent when seen face-on (central, face-on, optical depth $\tau_0 = 0.5-1.5$). Equivalent fits can be produced using faster radiative transfer models that neglect scattering. In the K'-band, no trace is found of a second, massive, dust disk, which has been invoked to explain observations of dust emission in the submillimeter. I discuss the model degeneracies and the effect of complex structures on the fitted distributions. In particular, most bulges in the sample show a box/peanuts morphology with large residuals; two lower-inclination galaxies show a dust ring distribution, which could be the cause of the large, fitted, dust scalelengths.

Key words. dust, extinction – galaxies: ISM – galaxies: stellar content – galaxies: spiral

1. Introduction

Edge-on spiral galaxies offer a unique opportunity to study the three-dimensional structure of disks: the vertical and radial behavior of the stellar distribution can be analyzed in a rather direct manner, provided the heavily extinguished dust lane is avoided and/or observations are taken in a band not strongly affected by dust (see, e.g. van der Kruit & Searle 1982; de Grijs & van der Kruit 1996; Pohlen et al. 2000b; Florido et al. 2001); the properties of the dust distribution can be inferred from the extinction lane itself. In this second case, however, the analysis requires three-dimensional models for the radiative transfer of starlight through dust, and these are computationally demanding, especially when proper geometries and scattering are taken into account.

To date, only Kylafis & Bahcall (1987) and Xilouris et al. (1997, 1998, 1999) have fitted the surface brightness distribution in edge-on spiral galaxies by using realistic radiative transfer models. In the works of Xilouris et al., two independent disks were used to describe the stellar and dust distribution (both having a radial and vertical exponential fall-off), to which a spheroidal distribution was added to model the bulge. After analyzing a sample of seven galaxies, Xilouris et al. (1999) concluded that the dust disk is thinner (vertically) but larger (radially) than the stellar. Its optical depth perpendicular to the disk is smaller than one in optical wavebands, making the disk almost transparent when seen face-on.

The dust disk emerging from the work of Xilouris et al. poses a problem, since such a structure cannot absorb more than 10% of the stellar radiation. Observations in the infrared, instead, show that ∼30% of the total bolometric emission of a spiral galaxy is radiated by dust (Popescu & Tuffs 2002) and thus has been absorbed from starlight. The conservation of this *energy balance* demands a larger amount of dust in the disk than what has been derived from optical images (Bianchi et al. 2000). The deficit in absorption is mitigated if a sizable fraction of starlight is assumed to suffer extinction within localized areas (i.e. star-forming region in molecular clouds) and not only diffuse extinction within the disk. Even taking this into account, models fail to predict the emission from the colder dust component in the FIR/sub-mm, so that a supplemental dust distribution is needed (Popescu et al. 2000; Misiriotis et al. 2001).

In the models for the edge-ons NGC 891 and NGC 5907, Popescu et al. (2000) and Misiriotis et al. (2001) include a second dust disk, associated with the younger stellar population. Being thinner than the disk resulting from the analysis of Xilouris et al., the second disk is not detectable in optical images, as its effects occur in a region already heavily affected by the extinction from the first, thicker disk. Nevertheless, the second dust disk is required to be a factor 2–3 more massive than the first. An alternative explanation for the model failures in the FIR/sub-mm is that the adopted dust emissivity, derived from the diffuse emission in the Milky Way, is underestimated by about a factor 3 (Dasyra et al. 2005).

To test the reliability of radiative transfer fitting techniques and to ascertain whether an extra dust disk component is indeed present, in this paper I analyze a sample of seven edge-on

---

[⋆] Based on observations made with the Italian Telescopio Nazionale Galileo (TNG) operated on the island of La Palma by the Fundación Galileo Galilei of the INAF (Istituto Nazionale di Astrofisica) at the Spanish Observatorio del Roque de los Muchachos of the Instituto de Astrofisica de Canarias

[⋆⋆] Figures 5 to 16 are only available in electronic form via `http://www.aanda.org`

Table 1. The sample.

name	T^a	D^b	PA ^{c}	RA Dec (J2000)^d
NGC 4013	3	14.5	244.8	11 58 31.3 +43 56 50.8
NGC 4217	3	16.9	49.3	12 15 51.1 +47 05 29.8
NGC 4302	5	20.2	50.8	12 21 42.3 +14 35 53.9
NGC 5529	5	41.9	294.1	14 15 34.2 +36 13 37.5
NGC 5746	3	26.6	350.2	14 44 56.1 +01 57 18.8
NGC 5965	3	47.4	52.6	15 34 02.4 +56 41 07.5
UGC 4277	6	76.5	109.5	08 13 57.1 +52 38 53.0

^{a} Morphology parameter (RC3). ^{b} Distance in Mpc, assuming H_0 = 73 km s^{-1} Mpc^{-1} and velocities w.r.t. the CMB dipole (from NED). ^{c} Position angle in degrees, from the V-band fit. ^{d} Galactic center, from the V-band fit.

galaxies, observed in the V and in the K' bands. The second dust disk should be discernible in NIR observations, due to its higher optical depth with respect to the thicker disk. Dasyra et al. (2005) analyzed a K_n-band image of NGC 891 and found an extinction lane consistent with a single disk model. In this work I will be able to do the same analysis with higher resolution and a deeper set of NIR images. The galaxies were selected because of the evident dust lane, their symmetrical appearance, and their closeness, so as to provide optimal ground for applying radiative transfer fitting techniques. They all have morphological type Sb to Sc. The sample is listed in Table 1. Two objects (NGC 4013 and NGC 5529) have been extensively analyzed in Xilouris et al. (1999): this will allow the uniqueness of the results of fitting procedures to be checked.

The paper is structured as follows: the observations are described in Sect. 2; the radiative transfer model and the procedure adopted for fitting are presented in Sect. 3; the results of fits to observations are shown in Sect. 4; finally, the main points are summarized and discussed in Sect. 5.

2. Observations and data reduction

Observations were carried out in March and April 2006, at the 3.5 m TNG (Telescopio Nazionale Galileo) telescope, located at the Roque de Los Muchachos Observatory in La Palma, Canary Islands.

The V-band images were obtained in dark time using the DOLORES instrument in imaging mode (Molinari et al. 1997). The pixel scale is $0.^{\prime\prime}275$ and the field of view $9.^{\prime}4 \times 9.^{\prime}4$, a size well-suited to the galaxies in the sample. For each object, three dithered exposures were taken, for a total of 750 s. Standard data reduction was carried out using the STARLINK package CCDPACK (Draper et al. 2002). As conditions during the observing nights were not photometric, calibration was achieved using the total V-band magnitude of the galaxies from RC3 (de Vaucouleurs et al. 1991). The sky noise in the V-band images is typically 25.8 mag arcsec^{-2} (1-σ) and the seeing $1.^{\prime\prime}8$ (FWHM).

The K'-band images were obtained with the NICS instrument in wide-field imaging (Baffa et al. 2001). Because of the smaller field of view ($4.^{\prime}2 \times 4.^{\prime}2$, with pixel scale $0.^{\prime\prime}25$), the camera was aligned with the galactic plane of each galaxy using the RC3 position angle; two overlapping fields were observed, each with an offset of $100''$ from the galactic center. Each field was observed with a dithered pattern of 12 on and off positions, each consisting of 6 short exposures of 20 s on the source (and on the sky) for a total exposure of 1440 s on source. Due to its smaller extent on the sky, only UGC 4277 required a single telescope pointing, with the galactic plane aligned with the camera diagonal. Data reduction was carried out with the dedicated software SNAP (Speedy Near-infrared data Automatic Pipeline; Mannucci et al., in preparation), which takes care of flat-fielding, sky subtraction, corrections for geometrical distortion and electronic effects, and final image mosaicing. Calibration was obtained from objects in the 2MASS point source catalog (Skrutskie et al. 2006). The sky noise in the K'-band images is typically 21.2 mag arcsec^{-2} (1-σ), about a magnitude deeper than in 2MASS Large Galaxy Atlas images (Jarrett et al. 2003). The seeing during observations was $1.^{\prime\prime}0$ (*FWHM*).

3. Modelling and fitting

The analysis presented in this work consists in producing a mock image of a galaxy and comparing it with the observed image by means of χ^2 minimization techniques, with the aim of deriving the parameters that better describe the object.

3.1. The galactic model

A standard description is adopted for the disk (see, e.g. Xilouris et al. 1999), an exponential (both along the radial coordinate r and the vertical coordinate z) with luminosity density (per unit solid angle)

$$\rho^{\rm disk}(r,z) = \frac{I_0^{\rm disk}}{2\,z_{\rm s}} \exp\left[-\frac{r}{h_{\rm s}} - \frac{|z|}{z_{\rm s}}\right], \qquad (1)$$

where $I_0^{\rm disk}$ is the disk *face-on* surface brightness through the galactic center and $h_{\rm s}$ and $z_{\rm s}$ are the radial and vertical scalelength.

For the bulge I used a de-projected Sersic profile of index n, with luminosity density given by

$$\rho^{\rm bulge}(r,z) = \frac{I_0^{\rm bulge}}{A_n\,R_{\rm e}\,b/a} \frac{\exp(-b_n\,B^{1/n})}{B^\alpha}, \qquad (2)$$

where $I_0^{\rm bulge}$ is the bulge *face-on* surface brightness through the galactic center, $R_{\rm e}$ the effective radius, b/a the minor/major axis ratio of the bulge,

$$B = \frac{\sqrt{r^2 + z^2/(b/a)^2}}{R_{\rm e}},$$

$$b_n = 2n - 1/3 - 0.009876/n, \qquad \alpha = (2n-1)/2n,$$

and A_n = 2.73, 3.70, 4.47, 5.12 for n = 1, 2, 3, 4, respectively (Prugniel & Simien 1997). When projected on the sky plane, Eq. (2) corresponds to a Sersic (1968) profile of index n. Traditionally, bulges in spiral galaxies have been described with the $R^{1/4}$ (de Vaucouleurs 1959) profile typical of elliptical galaxies (n = 4). Recent work, however (see, e.g. Hunt et al. 2004), suggests that bulges in late type galaxies tend to follow Sersic profiles with smaller n. Here I use n = 2 and 4.

The model includes a single dust disk with extinction coefficient given by

$$\kappa(r,z) = \frac{\tau_0}{2\,z_{\rm d}} \exp\left[-\frac{r}{h_{\rm d}} - \frac{|z|}{z_{\rm d}}\right], \qquad (3)$$

where τ_0 is the central, face-on, optical depth of the dust disk, and $h_{\rm d}$ and $z_{\rm d}$ are the radial and vertical scalelengths.

For computational reasons, the stellar disk is generally truncated along the radius at $4h_s$ and the dust disk at $4h_d$. Observations suggest that stellar disks follow the simple exponential decline of Eq. (1) up to about $4h_s$, although the truncation is not sharp and there is a large scatter in the measures (see the review in Pohlen et al. 2004). No indications are available for the dust disk. The stellar and dust disks are truncated vertically at $6z_s$ and at $6z_d$, while the bulge extends to 10 R_e.

The simulated image is created with the same pixel resolution and extent as the observed image with which it is compared. The geometrical parameters describing the appearance of the model galaxy on the image are θ, the inclination of the galactic z-axis with respect to the line of sight (l.o.s; $\theta = 90°$ for the pure edge-on case), the position of the projection of the galactic center on the sky and the position angle (PA). PA is defined so that, by rotating the galaxy counterclockwise by (90-PA) degrees, the projection on the sky of the positive z-axis of the galaxy lies along the positive y-axis on the image.

I used two radiative transfer models to produce simulated images. In the first, faster model, scattering is not taken into account. The extinction coefficient in Eq. (3) is taken to be entirely due to absorption. The image surface brightness is derived by analytic integration of the dust-attenuated stellar luminosity $\rho e^{-\tau}$ along the l.o.s. passing through the center of each image pixel (with the optical depth τ the integral of Eq. (3) from the location of stellar emission to the observer).

The second model is a Monte Carlo (MC) radiative transfer code including scattering. The basics of the method are presented in Bianchi et al. (1996). The code has been rewritten and optimized along the lines described in Baes et al. (2003). In particular, the *peeling-off* technique (Yusef-Zadeh et al. 1984) was implemented, producing images at a specific inclination θ rather than for a broad inclination band as in our original paper. As for the dust scattering properties, the albedo ω and asymmetry parameter g were taken from the Milky Way dust grain model of Weingartner & Draine (2001): for the V-band it is $\omega = 0.67$ and $g = 0.54$, for the K'-band, $\omega = 0.45$ and $g = 0.14$. The extinction law gives $A_{K'}/A_V = 0.12$. The Henyey & Greenstein (1941) phase function for scattering was used.

Finally, the model image is convolved with a Gaussian of appropriate FWHM to simulate the effect of seeing. This is important for reducing the central spike of the bulge, especially in the case of the analytic calculation where, contrary to MC images, the surface brightness is not smoothed over the pixel area.

3.2. The fitting procedure

Before proceeding to the fitting, stars and image defects were masked out from observations, together with all pixels lying out of the 3-σ isophote. The sky level, derived from regions free of sources, was subtracted. To speed up the fitting process, images were further smoothed and rebinned over 2 × 2 or 3 × 3 pixel, typically leaving 50 000 and 25 000 pixels available for the fit, in the V- and K'-band, respectively. Tests show that this further rebinning does not affect the fit.

For fits with the analytic no-scattering model, I tested both the Levenberg-Marquardt and the downhill simplex (the *amoeba* algorithm) minimization techniques (Press et al. 1996). The first is quicker, but only when the initial guesses for the parameters are close to the final values; otherwise, the technique tends to be trapped into local minima of the complex χ^2 surface. The *amoeba* algorithm, is instead able to converge, after successive restarts of the procedure, over minima that are quite distant, in parameter space, from the initial guess. When using the MC model, the *amoeba* method is mandatory, because the statistical nature of MC images does not allow quick computation of the derivatives required by the Levenberg-Marquardt method. In all cases, the fitting codes were implemented on a parallel machine. For the analytic method, calculations on groups of pixels are distributed among different *cpu*s and the results collected in the final image, while for the MC method, each *cpu* produces a whole image starting from an independent random seed, and all images are finally summed up to produce a higher signal-to-noise (S/N) result.

To summarize, the parameters obtained through the fit are twelve: $I_0^{\rm disk}$, h_s, z_s, $I_0^{\rm bulge}$, R_e, b/a, h_d, z_d, τ_0, θ, PA, and the center position. First, their values were estimated from cuts parallel and perpendicular to the disk plane, as described in Xilouris et al. (1997). Then, a no scattering fit was done, with successive calls of the *amoeba* and Levenberg-Marquardt methods, until a stable minimum was found. The final fit was achieved with the MC method, again with various calls of the *amoeba* method.

3.3. Testing the procedure

The fitting techniques were extensively tested on a large set of simulated images, covering a wide range of parameters. Simulated images were produced using the full MC model including dust scattering. The surface brightness in the models was scaled to the typical values in observations. The pixel size was also chosen to match the observations, and appropriate noise and seeing were added. Finally, the simulated images were prepared for fitting as described in Sect. 3.2. For illustrative purposes, I discuss here the results of tests on a model based on the NGC 891 fit of Xilouris et al. (1999). Simulations were made for the V- and K'-bands (the dust disk fitted to the V-band image was used in both cases, with $\tau_0^{K'}$ scaled according to the Milky Way extinction law) and for inclinations of 89.8° (the fitted galaxy inclination), 88°, and 86°.

In Fig. 1 I show the V-band surface brightness profiles of models (crosses) and fits (lines) for the three inclination cases. In each case, the profiles are obtained along three vertical cuts (perpendicular to the galactic plane) passing through the model center and at distances from the model of h_s and $2h_s$. As outlined in Sect. 3.2, fits were first produced with the no-scattering analytical model (dashed line), then the results used as starting point for the MC fit (solid line). The MC fits reproduce the data very well, and most of the input parameters can be retrieved with accuracies within 10%, gradually worsening for images of lower θ (whose value, even in the worst cases, is retrieved with an error of 2%). The values of R_e and $I_0^{\rm bulge}$ suffer the largest error (up to 20% and 40%, respectively, in the image with $\theta = 86°$).

Figure 1 also shows that the data can be reproduced equally well by the faster analytical fits that neglect scattering. The no-scattering fit can reproduce the surface brightness of a model including scattering with slight changes in the parameters, which are still derived with the same accuracy as discussed before (apart from z_d, $I_0^{\rm disk}$, and $I_0^{\rm bulge}$, which can have errors as high as 20%, 20%, and 50%, respectively). The optical depth τ_0 is underestimated (for a given optical depth, neglecting scattering results in an overestimate of the attenuation; Baes & Dejonghe 2001), but no more than 20%. In fact, the effects of scattering are minimal in edge-on galaxies (see, e.g. Bianchi et al. 1996).

Models in K'-band (see Fig. 2) have reduced extinction, so the presence of dust can only be inferred from small asymmetries along the minor axis direction. Therefore, it is more difficult to obtain the parameters of the dust disk: the fitted h_d, z_d, and τ_0

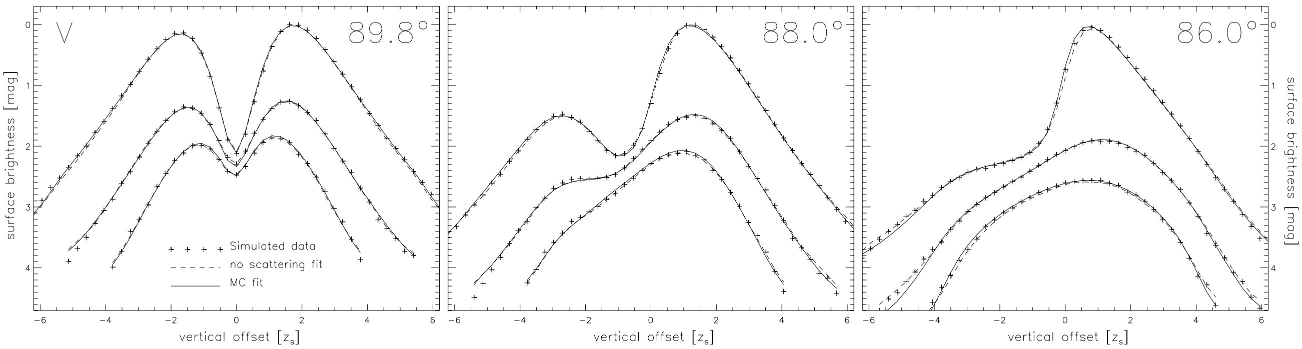

Fig. 1. V-band surface brightness profiles perpendicular to the galactic disk for the model and the fits described in Sect. 3.3. Three cuts are shown, at distances 0 (brightest profile), 1, and 2 $h_{\rm s}$ (dimmest profile) from the center along the galaxy's major axis.

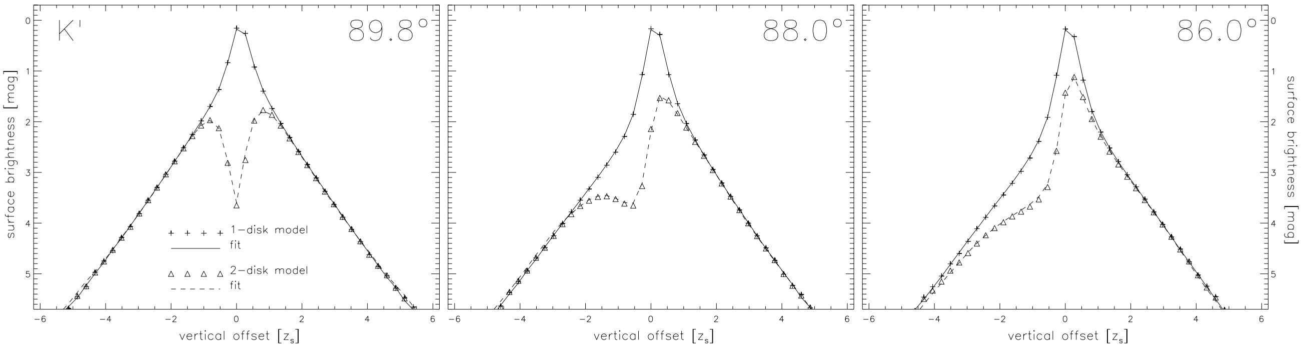

Fig. 2. K'-band surface brightness profiles along the minor axis for the models with a single dust disk and the model with two dust disks, together with their fits.

are within 20% of the input values. For the same reason, the parameters defining the stellar distributions are retrieved with slightly better accuracy than for the V-band case.

Other systematic effects were also explored using these simulations. Since only pixels with high S/N were chosen, a constant sky was subtracted from the images without attempting to fit its level. However, even assuming that the sky has been miscalculated by $\pm 3\sigma$, the parameters resulting from the fits are still very close to the input values, with the uncertainties quoted above. The same is true if the radial truncation of the stellar disk is varied within the estimates currently available from observations. I confirm the correlation observed by Pohlen et al. (2000a): an underestimate in the truncation of the stellar disk causes an overestimation of $h_{\rm s}$. Asymmetries and inhomogeneities in real images may hamper the correct determination of the inclination angle, especially for objects very close to edge-on: an overestimation of θ (so that the fit is more edge-on than the galaxy) would cause an overestimate of $z_{\rm s}$ and $z_{\rm d}$, leading also to larger $h_{\rm d}$ and smaller τ_0. It is worth noting that in the cases discussed here, where the parameters are deliberately kept fixed on different values from the input ones, the residuals in the fit are generally smaller than 20% for most (90%) of the data points. When dealing with real images, the deviations from the smooth model adopted here cause residuals on the same order or larger (Sect. 4). A large model degeneracy is thus possible.

Finally, I have added a second dust disk to the simulated images of NGC 891, following the recipes of Tuffs et al. (2004). Because a derivation of the parameters describing the second disk is not feasible, I studied its effects on the single dust-disk fitting model. The second, thin, dust disk has a central face-on, optical depth that is about 2.5 times that of the thick disk ($\tau_0 = 0.22$ in the thin disk vs. $\tau_0 = 0.09$ in the thick disk). As pointed out by (Popescu et al. 2000), its effects would not be easily discerned from those of the thick disk in the edge-on case. However, the second disk would be easily seen in all cases where the first produces a lower extinction, i.e. at lower θ and longer wavelength. Indeed, a deeper absorption trough is visible in V-band simulated images at all inclinations. It is also visible in K'-band simulations, as a deeper trough within 2° from the edge-on case and as a stronger minor axis asymmetry at lower inclination (see Fig. 2). As Fig. 2 shows, low-residual fits can be achieved in the K'-band, even if the simulated image includes a second dust disk. The parameters retrieved for the dust disk are now close to those of the second, more opaque, disk.

4. Results

For each galaxy in the sample, I show in Figs. 3 and 5 to 10 the image, the fit, and its residual for the V and K'-bands, respectively. Images have been processed as described in Sect. 3.2 and rotated counterclockwise by 90-PA. Cuts perpendicular and parallel to the galactic plane, through the center, and at different positions on the images, are shown in Figs. 4 and 11 to 16, for both bands. The best-fit parameters describing the stellar disk, the bulge, and the dust disk are listed in Table 2, together with the galaxy's inclination θ. The galactic center and the PA fitted to V and K' images generally agree within 1″ and 0°.5, respectively, and those derived for V images are shown in Table 1.

4.1. Global trends

The asymmetries and inhomogeneities in the stellar and dust distributions result in large residuals, which also highlight the presence of structures different from those adopted in Sect. 3.1. From a qualitative analysis of the fitted images and of the profiles, it appears that, in four objects (NGC 4013, NGC 4217, NGC 5529,

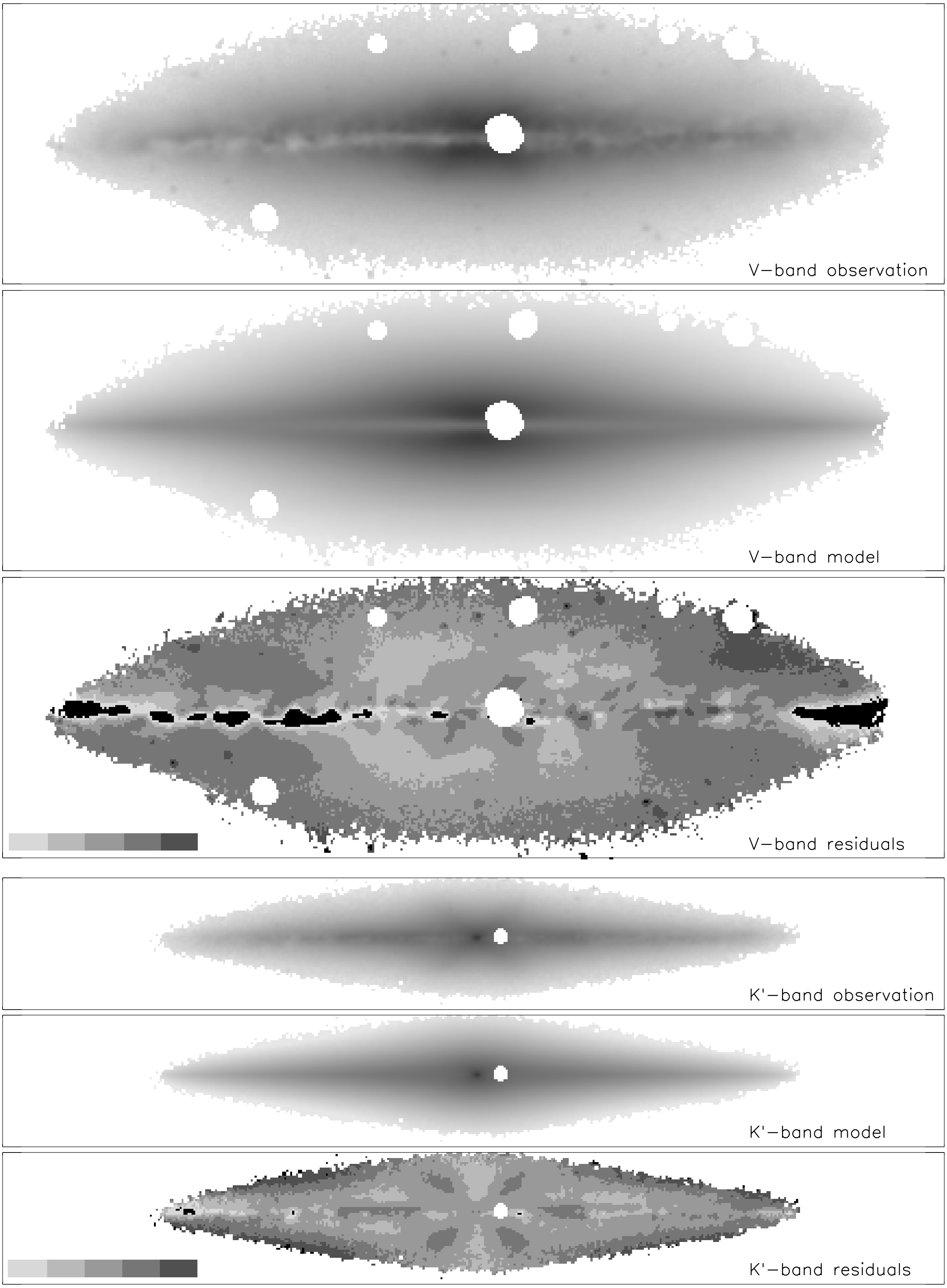

Fig. 3. NGC 4013. *From top to bottom*: the V-band image, the fit to the V-band image and the residuals; the K'-band image, the fit to the K'-band image and the residuals. Images and models are displayed with the modified logarithmic visualization method of Jarrett et al. (2003). The scale of residuals is linear: the bar with gray shades helps to distinguish regions with values in the ranges [–50%, –30%], [–30%, –10%], [–10%, 10%], [10%, 30%], and [30%, 50%] from lighter to darker. All regions with values outside these ranges are coded black. The horizontal size of the box is 6′.

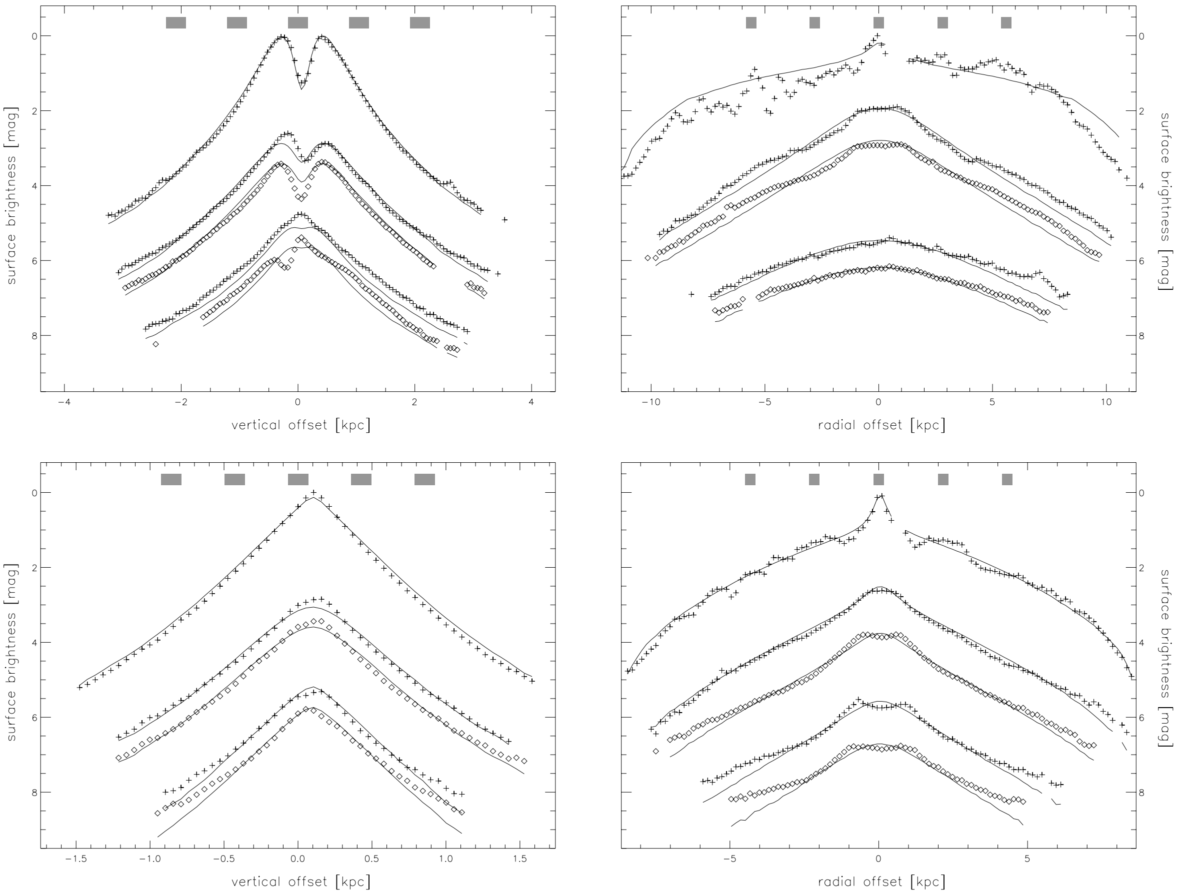

Fig. 4. NGC 4013. Surface brightness profiles for cuts perpendicular (*left panels*) and parallel (*right panels*) to the galactic disk, for the V-band (*top panels*) and the K'-band (*bottom panels*) images. In the left panels, profiles are shown for distances from the fitted center along the galactic plane corresponding to 0 (minor axis), ±1/8 and ±1/4 of the horizontal extent of the fitted area. Median values have been taken on a cut width of 2% that extent. The topmost data (crosses) refer to the minor axis, whose maximum has been assigned magnitude zero. Crosses refer to profiles on the right side of the images (with respect to Fig. 3) and are progressively displaced downward of 1.5 mag when moving from the center outward. Diamonds refer to the left side profiles, and are further displaced by 0.5 mag from their specular profile on the right side. The same scheme is adopted for the surface brightness profiles parallel to the major axis, shown in the right panels: profiles are shown for cuts at 0 (major axis; crosses), 1/8 and 1/4 of the vertical extent of the fitted area, above (crosses) and below (diamonds) the galactic plane. Median values have been taken over a cut width of 4% that extent. To reduce the cluttering of symbols only one point every three is plotted in horizontal profiles. Profiles are displaced in the same manner as in the left panels. In all panels, the curves refer to analogous cuts on the fitted images. Gaps in both model and data correspond to masked areas (i.e. stars). The shaded boxes in the upper part of the left (right) panels show the position and extent of the cuts displayed in the right (left) panels.

and UGC 4277) the model can describe the V images reasonably well, both for what concerns the stellar components and the extinction lanes produced by the dust disk. In two objects (NGC 5746 and NGC 5965) the fit is marginal with a good description of the general appearance of the stellar distributions, but with extinction features that are not reproduced by the model. In one object, NGC 4302, the fit is not able to describe the stellar distribution out of the galactic plane. In the K'-band, the general quality of the fits is similar to what it is in the V-band.

In a fit, the parameter that most quickly converges to the final value is the radial scalelength $h_{\rm s}$. In Table 2 the V-band $h_{\rm s}$ is given in kpc. To allow a ready comparison, all other scalelengths in Table 2 have been normalized to the V-band $h_{\rm s}$. The V-band $h_{\rm s}$ goes from about 3 kpc in the two bulge-dominated galaxies NGC 4013 and NGC 4217 to about 12 kpc in UGC 4277. Indeed, such a wide range for $h_{\rm s}$ has been found when fitting the surface brightness distribution in large samples of less inclined galaxies (de Jong 1996a; MacArthur et al. 2003).

The K'-band $h_{\rm s}$ is generally smaller than in the V-band, with a median ratio 0.75. This agrees with several works in the literature, that suggest that the reduction in $h_{\rm s}$ observed in low inclination galaxies when going from optical to NIR images is due to an intrinsic color gradient in the stellar population and not to the effects of dust extinction (de Jong 1996b; MacArthur et al. 2003; Möllenhoff 2004; Cunow 2004). A notable exception is that of Möllenhoff et al. (2006), which ascribe the increase in radial scalelengths from B to I to the optically thick second dust disk of Popescu et al. (2000). There is no evidence, instead, of a systematic difference between the vertical scalelength $z_{\rm s}$ in the V and K'-bands. In the V-band, it is $z_{\rm s}/h_{\rm s} \approx 0.1$, a result similar to what was obtained by Xilouris et al. (1999).

More delicate is the derivation of bulge parameters. For most objects, I used a spheroidal bulge with Sersic index $n = 2$, a choice appropriate for the morphological type of the galaxies considered here (Hunt et al. 2004). However, for two objects (NGC 4013 and NGC 4217) the $n = 2$ bulge was too steep to fit both the central peak and the ellipsoidal appearance of more external isophotes, so $n = 4$ was used in these cases. A spheroidal bulge appears to be a poor approximation to the real stellar distribution. In all but one object, positive residuals (i.e. model

Table 2. Fit results. $I_0^{\rm disk}$ and $I_0^{\rm bulge}$ are in mag arcsec^{-2}, the V-band $h_{\rm s}$ is in kpc, the K'-band $h_{\rm s}$, and all values for $z_{\rm s}$, $R_{\rm e}$, $h_{\rm d}$, and $z_{\rm d}$ are in units of the V-band $h_{\rm s}$. The Sersic index n is not fitted. The bulge-to-total light ratio B/T is computed from the stellar disk and bulge fit. The values for $h_{\rm d}$, $z_{\rm d}$, and θ are derived from the V-band fit and kept fixed in the K'-band fit.

	stellar disk			bulge					dust disk			
	$I_0^{\rm disk}$	$h_{\rm s}$	$z_{\rm s}$	$I_0^{\rm bulge}$	$R_{\rm e}$	b/a	B/T	n	$h_{\rm d}$	$z_{\rm d}$	τ_0	θ
NGC 4013 V	21.7	2.89	0.13	12.1	0.66	0.37	0.68	4	0.72	0.05	1.46	89.89
K'	16.9	0.75	0.09	9.1	0.49	0.55	0.27	4			0.15	
NGC 4217 V	20.7	3.31	0.06	13.0	1.31	0.29	0.59	4	1.75	0.10	1.26	88.01
K'	17.5	0.89	0.06	11.0	1.91	0.47	0.55	4			0.17	
NGC 4302 V	22.3	6.02	0.17	17.8	0.17	0.68	0.07	2	1.52	0.03	0.11	89.63
K'	17.4	0.56	0.08	10.1	0.01	0.54	0.02	2			0.01	
NGC 5529 V	21.2	7.26	0.08	17.4	0.47	0.49	0.21	2	1.36	0.03	0.68	86.94
K'	18.2	0.89	0.08	13.0	0.15	0.71	0.11	2			0.02	
NGC 5746 V	20.4	7.21	0.12	14.4	0.23	0.71	0.34	2	2.54	0.07	0.52	86.80
K'	17.7	0.99	0.13	11.7	0.18	0.65	0.24	2			0.05	
NGC 5965 V	21.6	9.69	0.10	15.2	0.21	0.72	0.39	2	1.82	0.02	0.62	84.43
K'	17.3	0.56	0.14	11.6	0.11	0.52	0.21	2			0.02	
UGC 4277 V	23.4	12.27	0.09	18.2	0.38	0.41	0.41	2	1.02	0.02	0.49	88.89
K'	18.4	0.61	0.07	12.8	0.11	0.71	0.19	2			0.02	

smaller than data) show "X"-like features in the fit to the K' or both bands. These features reveal families of orbits in which disk material is trapped by the perturbations caused by a bar (Patsis & Xilouris 2006), whose edge-on view causes a *boxy/peanut* appearance (Bureau et al. 2006). The deviations from the assumed bulge model are likely to affect also the derivation of both (i) $z_{\rm s}$, because the bulge and vertical disk structure contribute both to the surface brightness profile out of the disk plane near the center, and (ii) the parameters describing the dust disk, because the effects of dust extinction are more evident in the central part of the disk where the bulge contribution is sizable, if not dominant.

Excluding the bad, almost no-bulge, NGC 4302 fit, the $n = 2$ bulges have B/T ratios in the range 0.2–0.4 in the V-band, while the bulge contribution is larger in the two $n = 4$ fits. In the K'-band fit, the B/T ratio is always smaller than in the V-band, thus implying that the color of the bulges is *bluer* than the color of the disks. This is puzzling, since in contrast to what is generally found in the bulge/disk decomposition of less inclined objects (see, e.g. Möllenhoff 2004). However, a similar variation in the B/T ratios can be inferred from the fit of edge-on galaxies in Xilouris et al. (1999).

The dust disks fitted to the V-band images appear to be consistent with those derived by Xilouris et al. (1999), although the spread in values is wider. Generally, the radial scalelength $h_{\rm d}$ is longer than the stellar ($h_{\rm d}/h_{\rm s} \sim 1.5$), while the vertical scalelength $z_{\rm d}$ is shorter than $z_{\rm s}$ ($z_{\rm s}/z_{\rm d} \sim 3$). This last condition is necessary to produce the well-defined extinction lanes along the galactic disk. The disk opacity is moderate with a V-band τ_0 in the range 0.5–1.5, making the galaxies almost transparent when seen face-on (Xilouris et al. 1999).

The extinction features in K' images are not prominent and result mostly in weak asymmetries along the minor axis and in clumpy structures. The asymmetries due to dust cannot be easily distinguished by those due to deviations from the adopted models. In most cases, a free fit would converge to a dust-free model. Thus, the fits have been achieved by allowing only τ_0 to vary, while fixing both dust-disk scalelengths, $h_{\rm d}$ and $z_{\rm d}$, and the inclination θ to the result of the V-band fit. Low values for τ_0, in the range 0.02–0.15 were found. Such opacities only produces minimal extinction effects on the model (see, e.g. the solid lines in Fig. 2).

Instead, no extinction lanes associated to a thin, massive dust disk have been found. If the extra dust component supposed by Popescu et al. (2000) exists, it does not appear to be in the form of a second, smooth dust disk, which would produces features more easily discernible (see, e.g., the dashed lines in Fig. 2). The result agrees with the analysis of a K_n-band image of NGC 891 by Dasyra et al. (2005).

4.2. Comments on individual galaxies[1]

NGC 4013: the fit is generally good for both bands, with residuals smaller than 30% in 85% of the fitted data points. The dust lane can be seen easily in both bands. It shows a clumpy structure that leads to larger residuals along the major axis, especially in the V-band. A bulge with Sersic index $n = 4$ was used for this object. The V-band fit has similar parameters to those obtained by Xilouris et al. (1999), with the exception of $h_{\rm d}$, which I find to be smaller than $h_{\rm s}$, rather than larger. This also leads to the larger τ_0^V obtained here.
NGC 4217: the same considerations as for NGC 4013 apply to this object. The geometrical parameters of the stellar and dust disk, together with θ, are given for the B-band by Alton et al. (2000): the fit here is more edge-on and $h_{\rm d}$ is larger by 30%, while $h_{\rm s}$ is consistent with their fit. The difference in θ is also the cause of the smaller $z_{\rm s}$ I obtain. For this object I also have $z_{\rm d} > z_{\rm s}$: since the bulge dominates the surface brightness apart from regions close to the galactic plane, an extinction lane can appear even if the dust disk is thicker that the stellar. The major axis profiles clearly show a steepening of the profile beyond 10 kpc. This is the signature of a Type II truncation (in the notation of Pohlen & Trujillo 2006), which cannot be reproduced by

---

[1] All literature data have been scaled to the distances listed in Table 1.

the sharp cut used in the model. A truncation at the same distance is also found in the K_s-band by Florido et al. (2001), although the value of h_s they obtain is 40% higher than in the present fit. Dust extinction can be seen in the K'-band image, although not in the form of a dust lane but rather as a y-axis asymmetry in images, because of the inclination that is smaller than edge-on.

NGC 4302: this is the hardest object to fit, because of the major axis asymmetry around the center, the presence of a surface brightness contribution from the nearby face on galaxy NGC 4298 (whose center is at about 2.′3 from the galactic plane in the direction of the negative y axis in Fig. 6), and because of the complex vertical structure. Indeed, the model does not represent the observed surface brightness well, especially in the V-band. The contribution of the fitted bulge is negligible. It appears that there is a second thicker stellar disk (of V-band vertical scalelength 1.5 kpc, a quarter of the fitted h_s), with radial scalelength increasing with the distance from the galactic plane. Extinction in K' appears clumpy and does not alter the symmetry above the plane significantly.

NGC 5529: apart from a slight warp in the external part of the disk, a fit can be achieved, with residuals smaller than 30% in 70% of the data points. The fit of the disk is consistent with the analysis of a V-band image in Xilouris et al. (1999). Only tenuous, clumpy extinction can be seen in the K' image.

NGC 5746: the fit quality is the same as for NGC 5529 in both bands. The fit to the extinction lane in the V-band, though, is poorer. The parameters for the stellar and dust disks are not consistent with those reported for the B-band by Alton et al. (2000), with h_s larger by 40% in the present case. Extinction is located in a clumpy ring structure of radius ≈1.′3, which is evident in the K' image. From the ring in K', an inclination $\theta = 86° \pm 1°$ can be estimated, which is consistent with the fitted value.

NGC 5965: the galaxy is warped, with the outer disk and a ring-like dust lane on a different plane with respect to the inner peanut-shaped bulge. The stellar ring is evident in the K' image, while no extinction features can be detected. As with NGC 5746, the fit to the extinction lane in the V-band is poor, even though the global fit quality is not very different from the other objects. An estimate for h_s is available for the K_s-band, which is about 20% smaller than the present value (Bizyaev & Mitronova 2002). The fitted θ is consistent with the aspect of the K' ring, which suggests $\theta = 83.5° \pm 1.5°$.

UGC 4277: the fit is good, with 90% of the data points fitted by the model with residuals smaller than 30%. While the dust lane is evident for this nearly edge-on object in the V-band, only a weak asymmetry can be seen in the K'-band for the bulge above and below the galactic plane. The K_s-band value for h_s derived by Bizyaev & Mitronova (2002) is consistent with the result of the present fit.

5. Summary and discussion

In the present work a sample of seven nearby edge-on galaxies, observed in the V and K'-bands, has been analyzed using a radiative transfer model, in order to constrain the parameters describing the stellar and dust distributions. The dust and stellar disks were fitted with two smooth, independent exponential disks, and the bulge with a spheroidal distribution following Sersic profiles with $n = 2$ and 4. Hereafter I summarize and discuss the main results of the work.

(i) When applying the fitting technique to mock images of the same extent and S/N as the observations, it became evident that the parameters cannot be constrained better than a few tens of percent, because of the model degeneracies. In particular, it is possible to obtain good fits even when using a faster radiative transfer model that neglects scattering. For V-band models, this leads only to a small underestimation of the dust disk opacity and to variation in the other fitted parameters within the accuracy of full fits including scattering. Furthermore, the differences between scattering and non scattering models are smaller than the typical residuals obtained in fits of real images.

(ii) In the V-band, the parameters obtained for the dust disk are generally consistent with those derived by Xilouris et al. (1999) on a different sample of objects. The dust disk has a longer radial scalelength than stars ($h_\mathrm{d}/h_\mathrm{s} \sim 1.5$), a smaller vertical scalelength ($z_\mathrm{d}/z_\mathrm{s} \sim 1/3$), and is almost transparent when seen face-on ($\tau_0 = 0.5{-}1.5$). However, discrepancies exist when fits to single objects are compared to other works in the literature, possibly a result of different models, fitting techniques and image coverage. It is worth noting that the highest values for h_d were obtained for two objects, NGC 5746 and NGC 5965, which clearly show the presence of a ring structure in the K'-band image. If dust is distributed in a ring (indeed, extinction along the ring is seen in the K' image of NGC 5746), the displacement of the maximum extinction out of the center of the galaxy could be the reason for the larger h_d, when the fit is performed using the simple exponential disk of Eq. (3).

A similar effect could be caused by the more external clouds, if the clumpy structure of the dust disk dominates its smooth component. Misiriotis & Bianchi (2002) analyzed the effects of clumping on radiative transfer fits and concluded that a clumpy distribution leads to a *smaller* h_d. The different result may, however, be due to the fact that their model was unable to produce high-resolution images with discernible dust clouds.

(iii) The properties of the stellar disk are similar to those derived from bulge/disk decomposition of less inclined galaxies. In particular, the stellar disk has a larger h_s in the V-band than in the K'-band, suggesting that the color gradient along disks is due to the intrinsic properties of the stellar populations rather than to the effect of extinction. The bulge component proved to be more complex than the assumed spheroidal model, with an "X"-like residual betraying a box/peanut morphology in all but one galaxy. I warn here that the departure of the bulge shape from model assumptions can cause uncertainties in the derivation of the dust disk properties, since the extinction lane is deeper in regions where the bulge contributes most.

(iv) Images in the K'-band show little dust extinction, mostly consisting in minor axis asymmetries and in clumpy structures. I found no trace of the second, thinner, more massive, and smooth dust disk introduced by Popescu et al. (2000) and Misiriotis et al. (2001) to explain the sub-mm dust emission in NGC 891 and NGC 5907. Since the problem of the discrepancy in *energy balance* persists between the radiation absorbed by dust from stars and that emitted in the infrared, we are left with the second hypothesis in Popescu et al. (2000): most of dust could be distributed in optically thick quiescent or star-forming clouds. Furthermore, dust in dense clouds could have a larger emissivity than what usually assumed for Milky Way dust, thus relieving part of the discrepancy in energy balance; see, e.g. Dasyra et al. (2005) for an alternative solution to the deficiency of sub-mm emission in models of edge-on galaxies. Realistic models for dust emission in a complex disk are needed, in order to ascertain the relative contribution of diffuse and clumpy dust to the infrared spectral energy distribution.

Clearly, the uncertainties in deriving of the structure of the dust disk could be reduced by using a dust tracer that is more *direct* than its extinction on starlight. In particular, observations of dust emission in the sub-mm appear to be easier to interpret in terms of dust density, because of the relatively high resolution and of the small dependence of the Rayleigh-Jeans spectrum on the dust temperature gradient. In the next few years, the advent of high-sensitivity, second-generation sub-mm bolometer-arrays like SCUBA-2 (Holland et al. 2006) and LABOCA (Kreysa et al. 2003), will allow observations of spirals over a much wider extent along the disk than previously possible. Equally important are the infrared observations of nearby galaxies carried on with the Spitzer satellite: a large number of nearby spirals have been already observed for the SINGS survey (Kennicutt et al. 2003), and analysis is ongoing on a sample of local edge-on objects (Roelof de Jong and Benne Holwerda, private communication). Very promising for a high-resolution study of the dust distribution appears to be the correlation between the PAHs emission, the ISM density (Regan et al. 2006), and the sub-mm emission (Haas et al. 2002).

Acknowledgements. I am grateful to several people for their suggestions and help during the observations and the analysis conducted for this work: Emmanuel Xilouris, Filippo Mannucci, Edvige Corbelli, Andrea Ferrara, Francesca Ghinassi, Carlo Giovanardi, Leslie Hunt, and Raffaella Schneider. This publication makes use of data products from the Two Micron All Sky Survey, which is a joint project of the University of Massachusetts and the Infrared Processing and Analysis Center/California Institute of Technology, funded by the National Aeronautics and Space Administration and the National Science Foundation. This research has made use of the NASA/IPAC Extragalactic Database (NED) which is operated by the Jet Propulsion Laboratory, California Institute of Technology, under contract with the National Aeronautics and Space Administration.

References

Alton, P. B., Rand, R. J., Xilouris, E. M., et al. 2000, A&AS, 145, 83
Baes, M., & Dejonghe, H. 2001, MNRAS, 326, 733
Baes, M., Davies, J. I., Dejonghe, H., et al. 2003, MNRAS, 1081
Baffa, C., Comoretto, G., Gennari, S., et al. 2001, A&A, 378, 722
Bianchi, S., Ferrara, A., & Giovanardi, C. 1996, ApJ, 465, 127
Bianchi, S., Davies, J. I., & Alton, P. B. 2000, A&A, 359, 65
Bizyaev, D., & Mitronova, S. 2002, A&A, 389, 795
Bureau, M., Aronica, G., Athanassoula, E., et al. 2006, MNRAS, 370, 753
Cunow, B. 2004, MNRAS, 353, 477
Dasyra, K. M., Xilouris, E. M., Misiriotis, A., & Kylafis, N. D. 2005, A&A, 437, 447
de Grijs, R., & van der Kruit, P. 1996, A&AS, 117, 19
de Jong, R. 1996a, A&A, 313, 45
de Jong, R. 1996b, A&A, 313, 377
de Vaucouleurs, G. 1959, Handbuck der Physik, ed. S. Flugge, Vol. 53 (Berlin: Springer), 275
de Vaucouleurs, G., de Vaucouleurs, A., Corwin, Herold, G. J., et al. 1991, Third Reference Catalogue of Bright Galaxies (Berlin: Cambridge University Press), RC3
Draper, P. W., Taylor, M., & A. A. 2002, Starlink User Note 139.16
Florido, E., Battaner, E., Guijarro, A., Garzón, F., & Jiménez-Vicente, J. 2001, A&A, 378, 82
Haas, M., Klaas, U., & Bianchi, S. 2002, A&A, 385, L23
Henyey, L. G., & Greenstein, J. L. 1941, ApJ, 93, 70
Holland, W., MacIntosh, M., Fairley, A., et al. 2006, in Millimeter and Submillimeter Detectors and Instrumentation for Astronomy III., Vol. 6275
Hunt, L. K., Pierini, D., & Giovanardi, C. 2004, A&A, 414, 905
Jarrett, T. H., Chester, T., Cutri, R., Schneider, S. E., & Huchra, J. P. 2003, AJ, 125, 525
Kennicutt, R. C., Jr., Armus, L., et al. 2003, PASP, in press
Kreysa, E., Bertoldi, F., Gemuend, H.-P., et al. 2003, in Millimeter and Submillimeter Detectors for Astronomy, ed. T. G. Phillips, & J. Zmuidzinas, 4855, 41
Kylafis, N. D., & Bahcall, J. N. 1987, ApJ, 317, 637
MacArthur, L. A., Courteau, S., & Holtzman, J. A. 2003, ApJ, 582, 689
Misiriotis, A., & Bianchi, S. 2002, A&A, 384, 866
Misiriotis, A., Popescu, C. C., Tuffs, R., & Kylafis, N. D. 2001, A&A, 372, 775
Molinari, E., Conconi, P., & Pucillo, M. 1997, Mem. Soc. Astron. It., 68, 231
Möllenhoff, C. 2004, A&A, 415, 63
Möllenhoff, C., Popescu, C. C., & Tuffs, R. J. 2006, A&A, 456, 941
Patsis, P. A., & Xilouris, E. M. 2006, MNRAS, 366, 1121
Pohlen, M., & Trujillo, I. 2006, A&A, 454, 759
Pohlen, M., Dettmar, R. J., & Lütticke, R. 2000a, A&A, 357, L1
Pohlen, M., Dettmar, R. J., Lütticke, R., & Schwarzkopf, U. 2000b, A&AS, 144, 405
Pohlen, M., Beckman, J. E., Huettemeister, S., et al. 2004, in Penetrating Bars through Masks of Cosmic Dust, ed. D. Block, I. Freeman, K. C. Puerari, & R. Groess (Kluwer)
Popescu, C. C., & Tuffs, R. J. 2002, MNRAS, 335, L41
Popescu, C. C., Misiriotis, A., Kylafis, N. D., Tuffs, R. J., & Fischera, J. 2000, A&A, 362, 138
Press, W. H., Teukolsky, S. A., Vetterling, W. T., & Flannery, B. P. 1996, Numerical Recipes in Fortran 90 (Cambridge University Press)
Prugniel, P., & Simien, F. 1997, A&A, 321, 111
Regan, M. W., Thornley, M. D., Vogel, S. N., et al. 2006, ApJ, 652, 1112
Sersic, J. L. 1968, Atlas de galaxias australes (Cordoba, Argentina: Observatorio Astronomico, 1968)
Skrutskie, M. F., Cutri, R. M., Stiening, R., et al. 2006, AJ, 131, 1163
Tuffs, R. J., Popescu, C. C., Völk, H. J., Kylafis, N. D., & Dopita, M. A. 2004, A&A, 419, 821
van der Kruit, P. C., & Searle, L. 1982, A&A, 110, 61
Weingartner, J. C., & Draine, B. T. 2001, ApJ, 548, 296
Xilouris, E. M., Kylafis, N. D., Papamastorakis, J., Paleologou, E. V., & Haerendel, G. 1997, A&A, 325, 135
Xilouris, E. M., Alton, P. B., Davies, J. I., et al. 1998, A&A, 331, 894
Xilouris, E. M., Byun, Y. I., Kylafis, N. D., Paleologou, E. V., & Papamastorakis, J. 1999, A&A, 344, 868
Yusef-Zadeh, F., Morris, M., & White, R. L. 1984, ApJ, 278, 186

Online Material

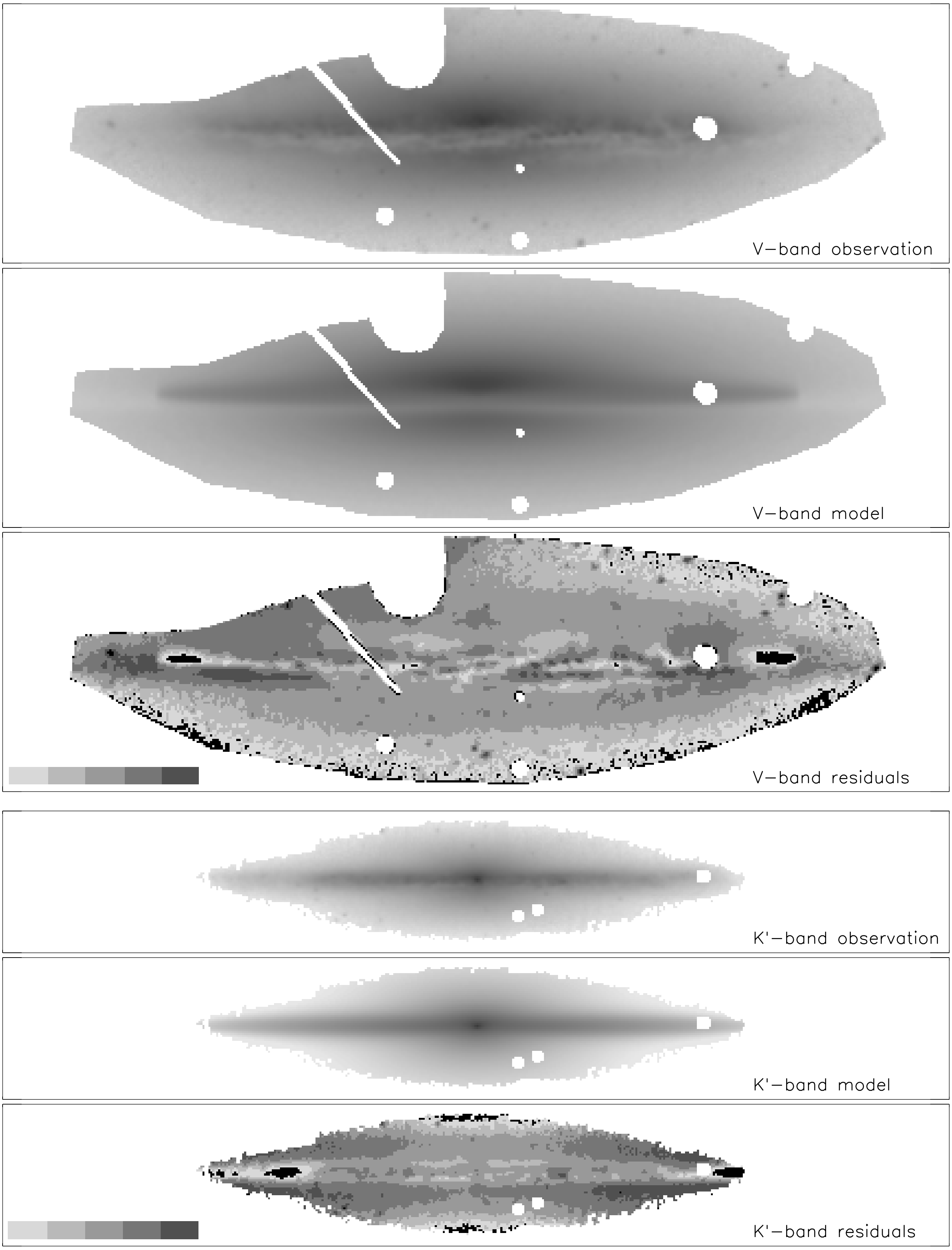

Fig. 5. NGC 4217. Image order is the same as in Fig. 3. The horizontal size of the box is 8′.

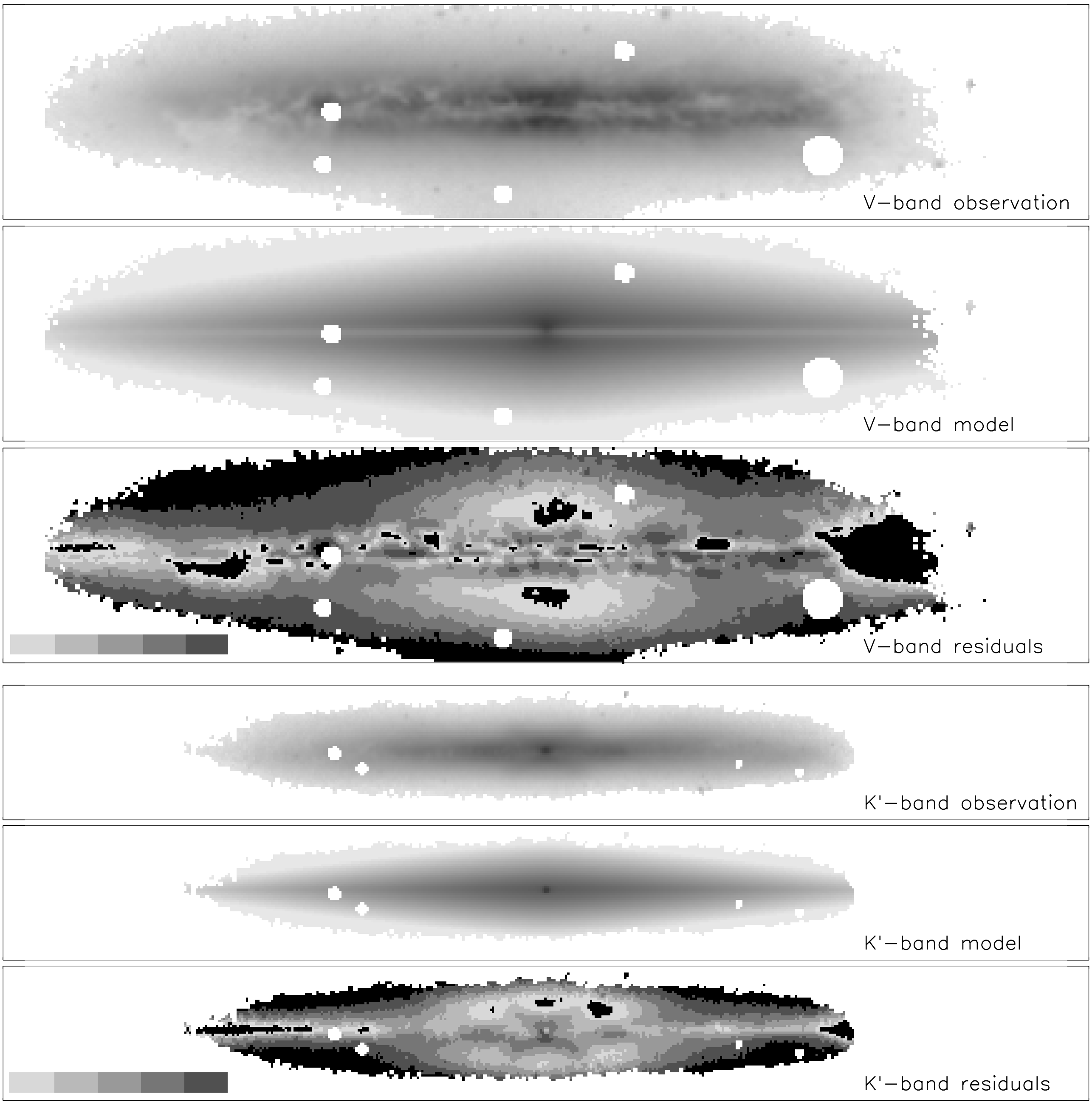

Fig. 6. NGC 4302. Image order is the same as in Fig. 3. The horizontal size of the box is 8′.

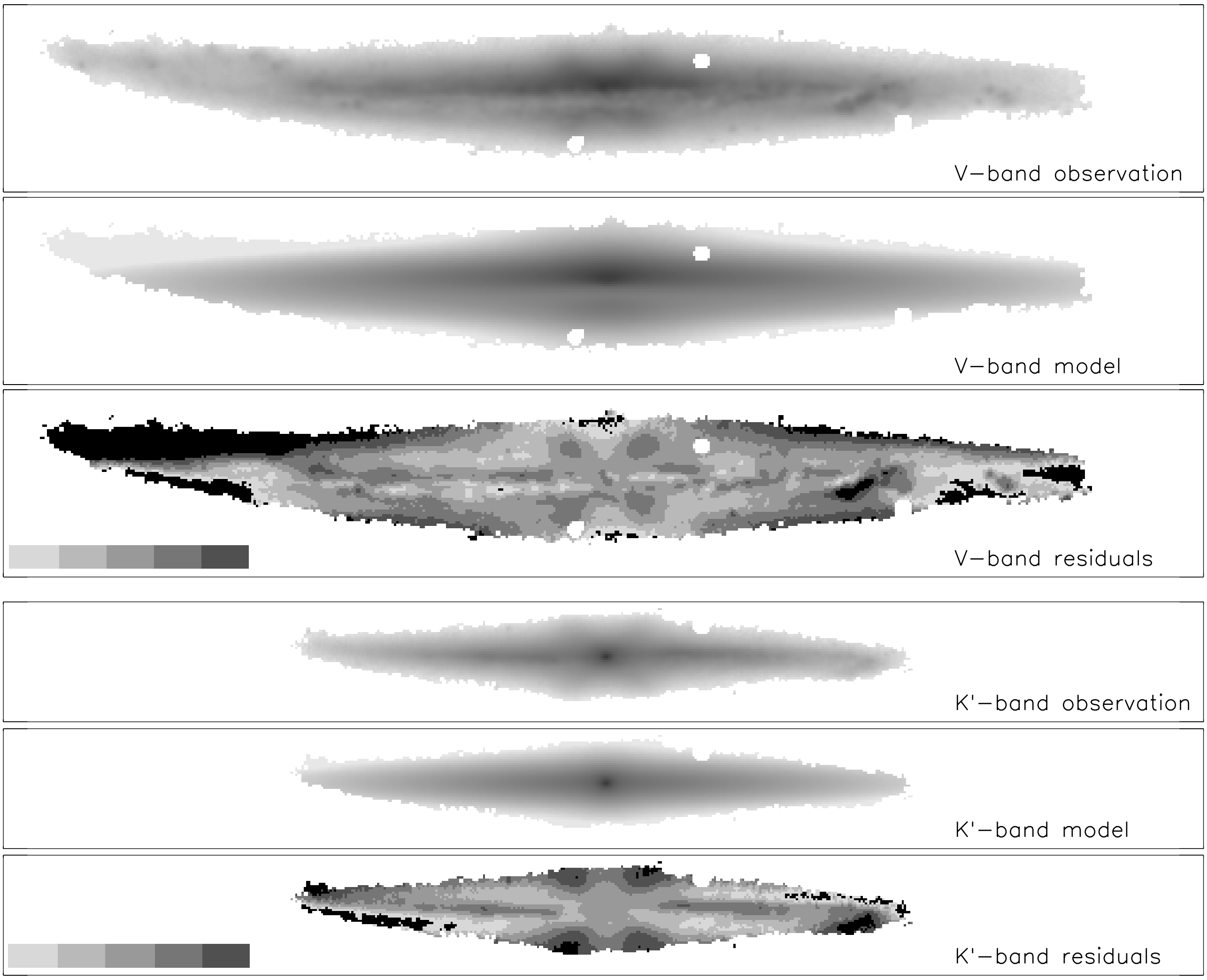

Fig. 7. NGC 5529. Image order is the same as in Fig. 3. The horizontal size of the box is 7′.

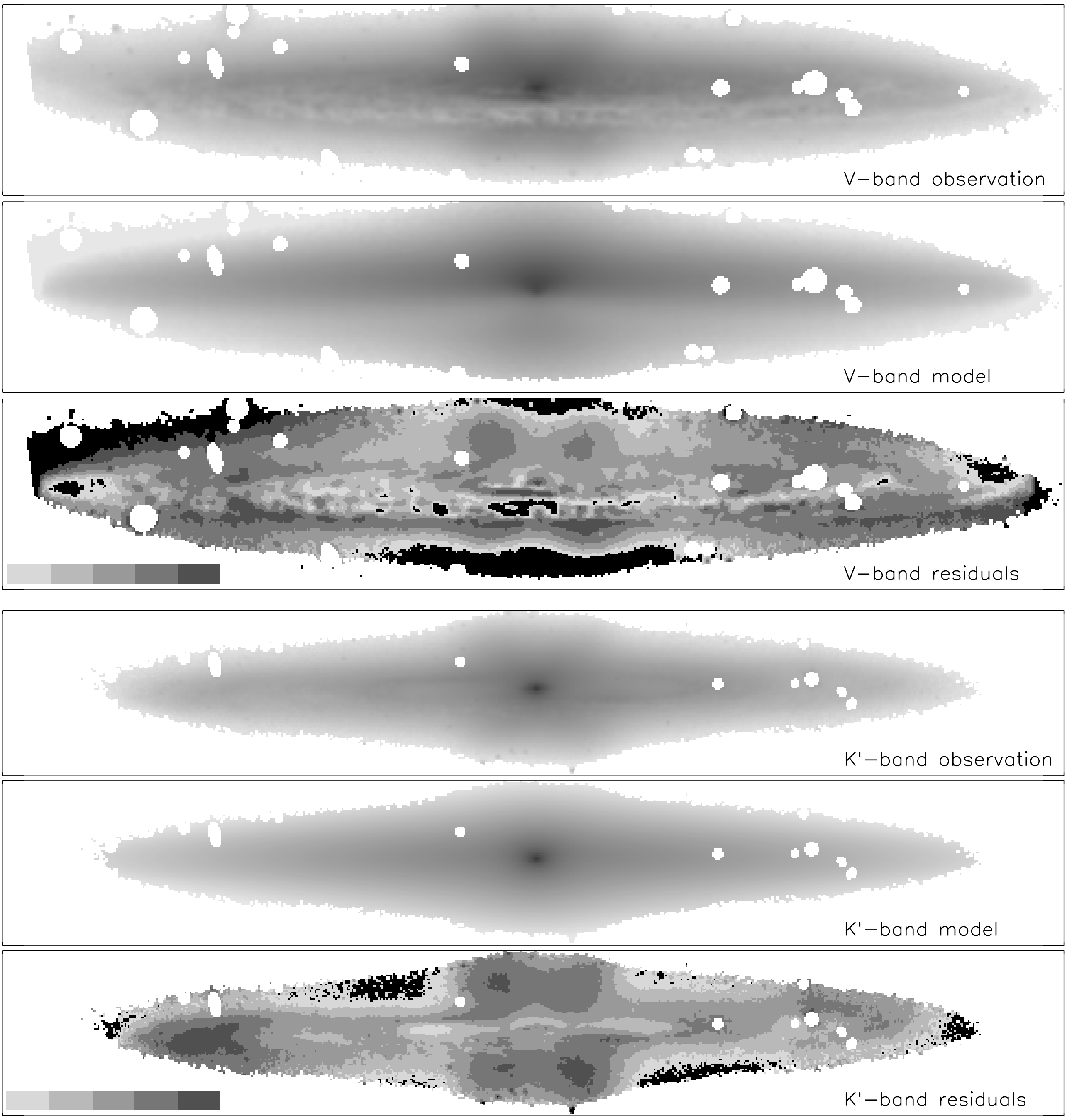

Fig. 8. NGC 5746. Image order is the same as in Fig. 3. The horizontal size of the box is 8′.

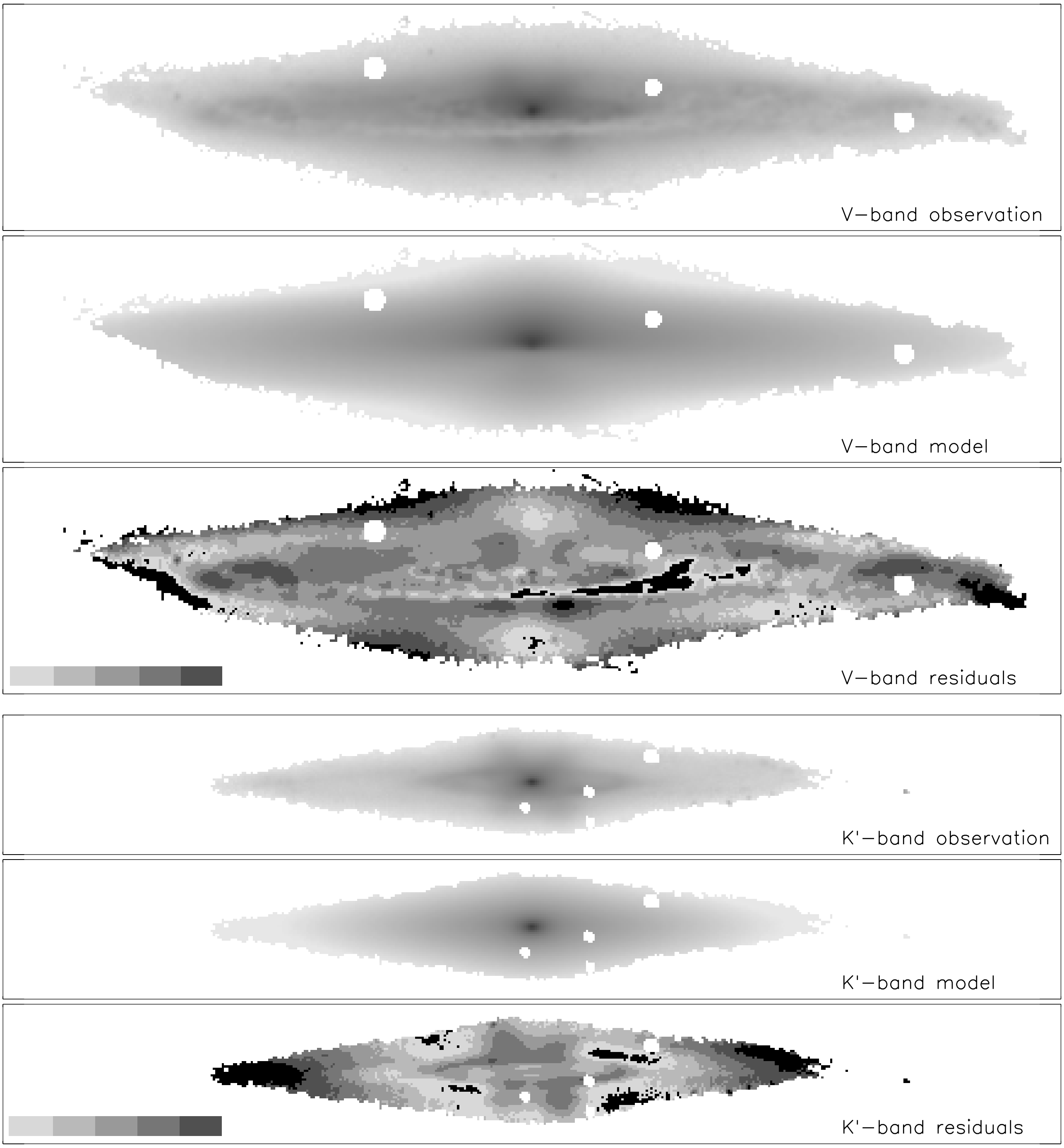

Fig. 9. NGC 5965. Image order is the same as in Fig. 3. The horizontal size of the box is 6′.

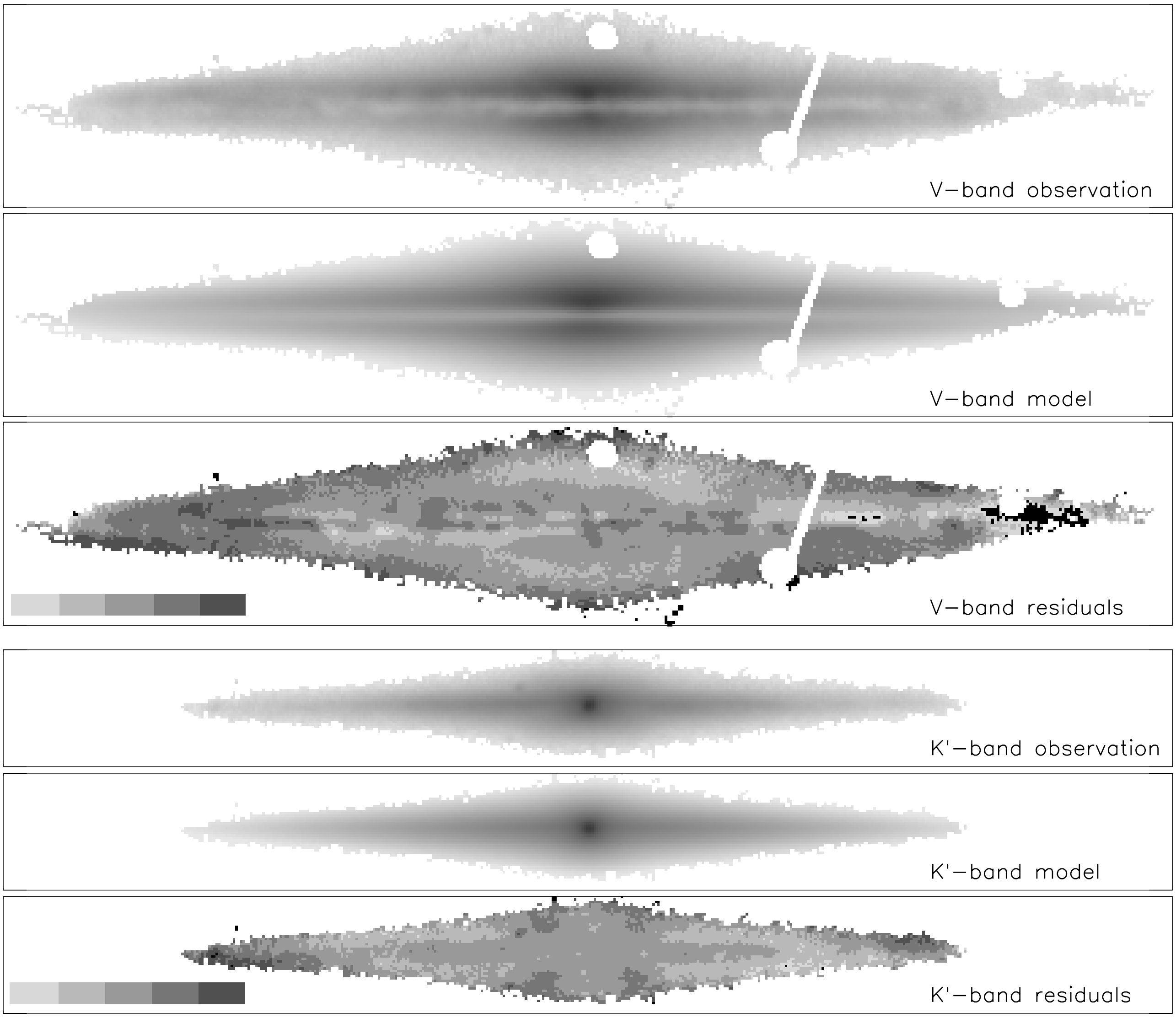

Fig. 10. UGC 4277. Image order is the same as in Fig. 3. The horizontal size of the box is 4′.

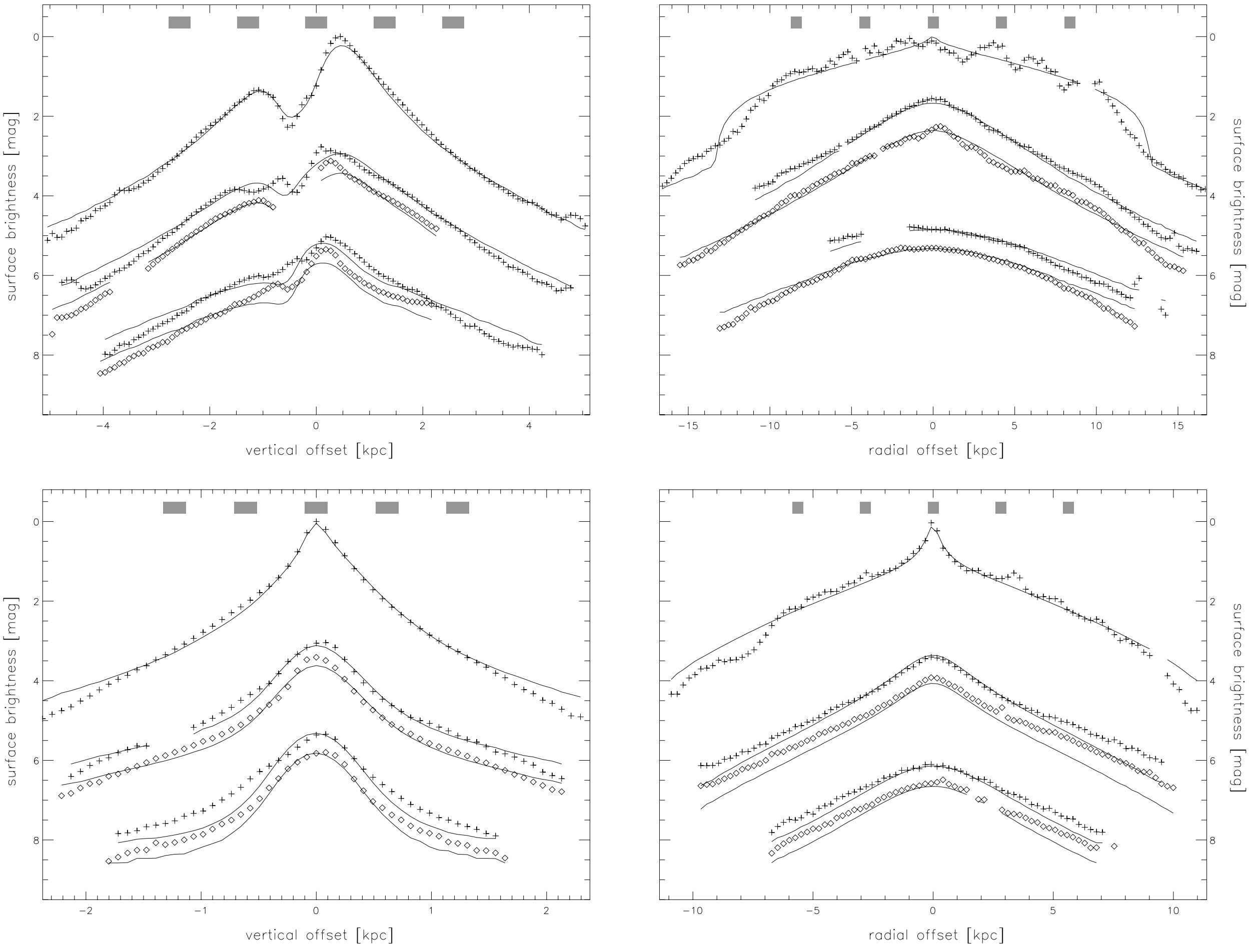

Fig. 11. Same as Fig. 4, but for NGC 4217.

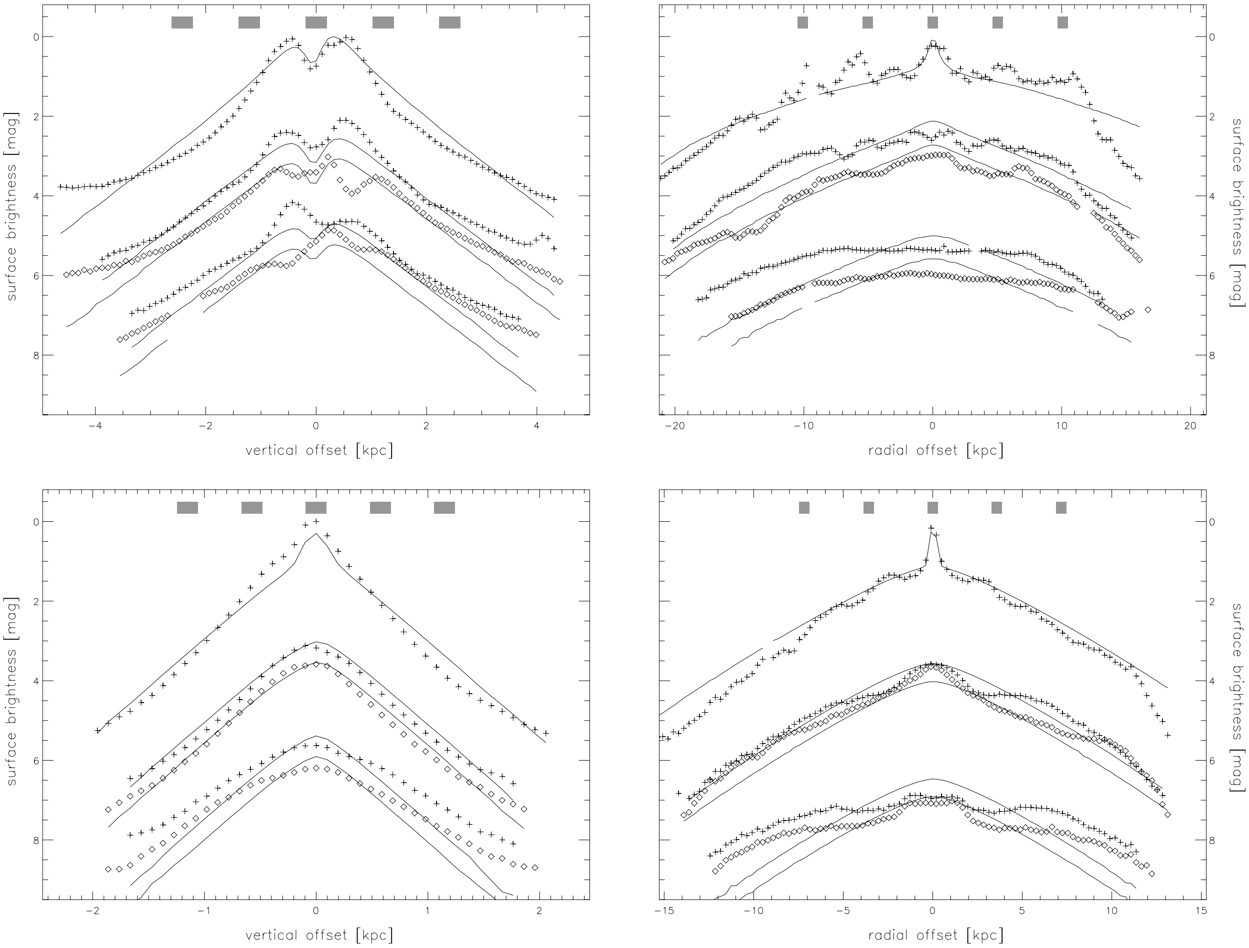

Fig. 12. Same as Fig. 4, but for NGC 4302.

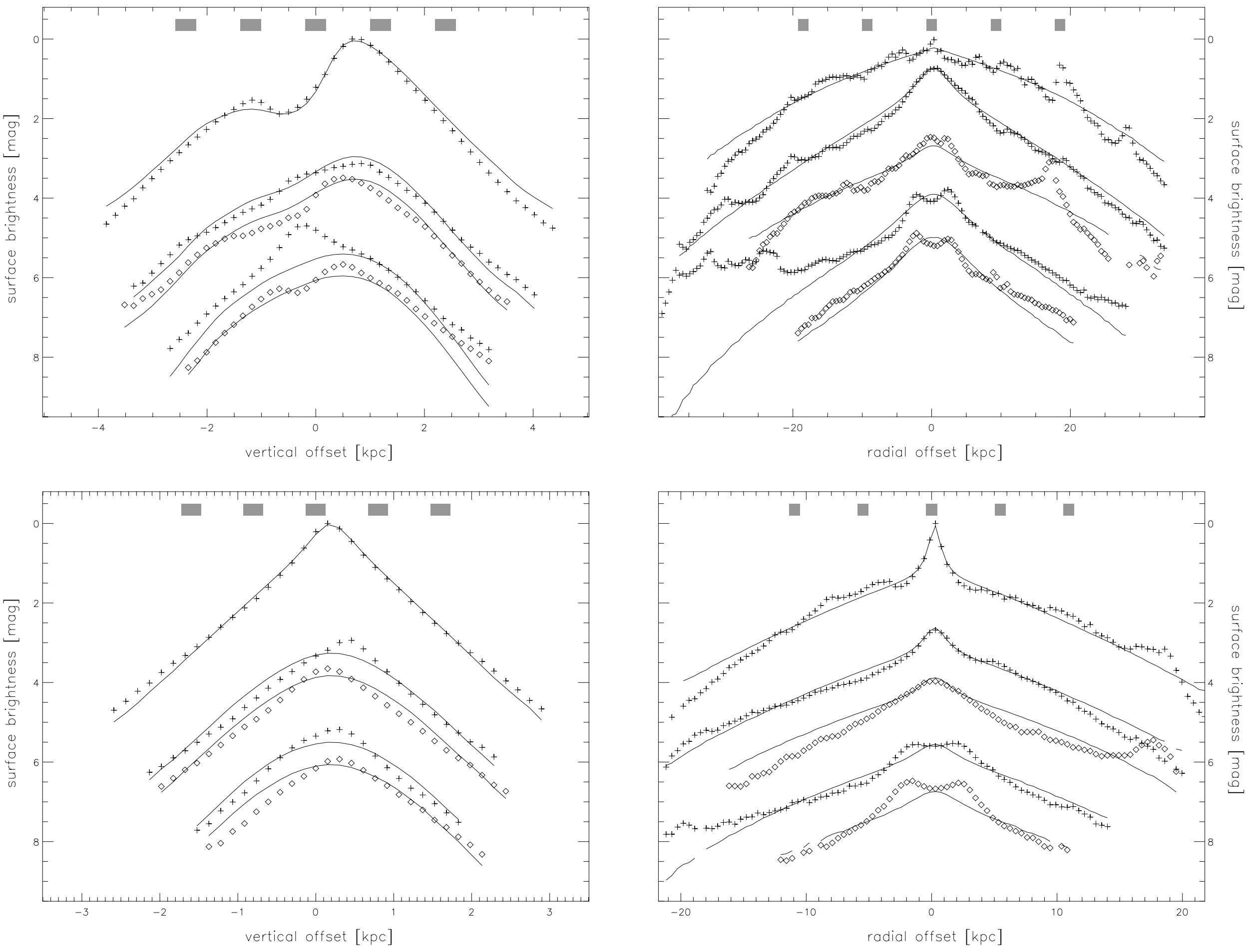

Fig. 13. Same as Fig. 4, but for NGC 5529.

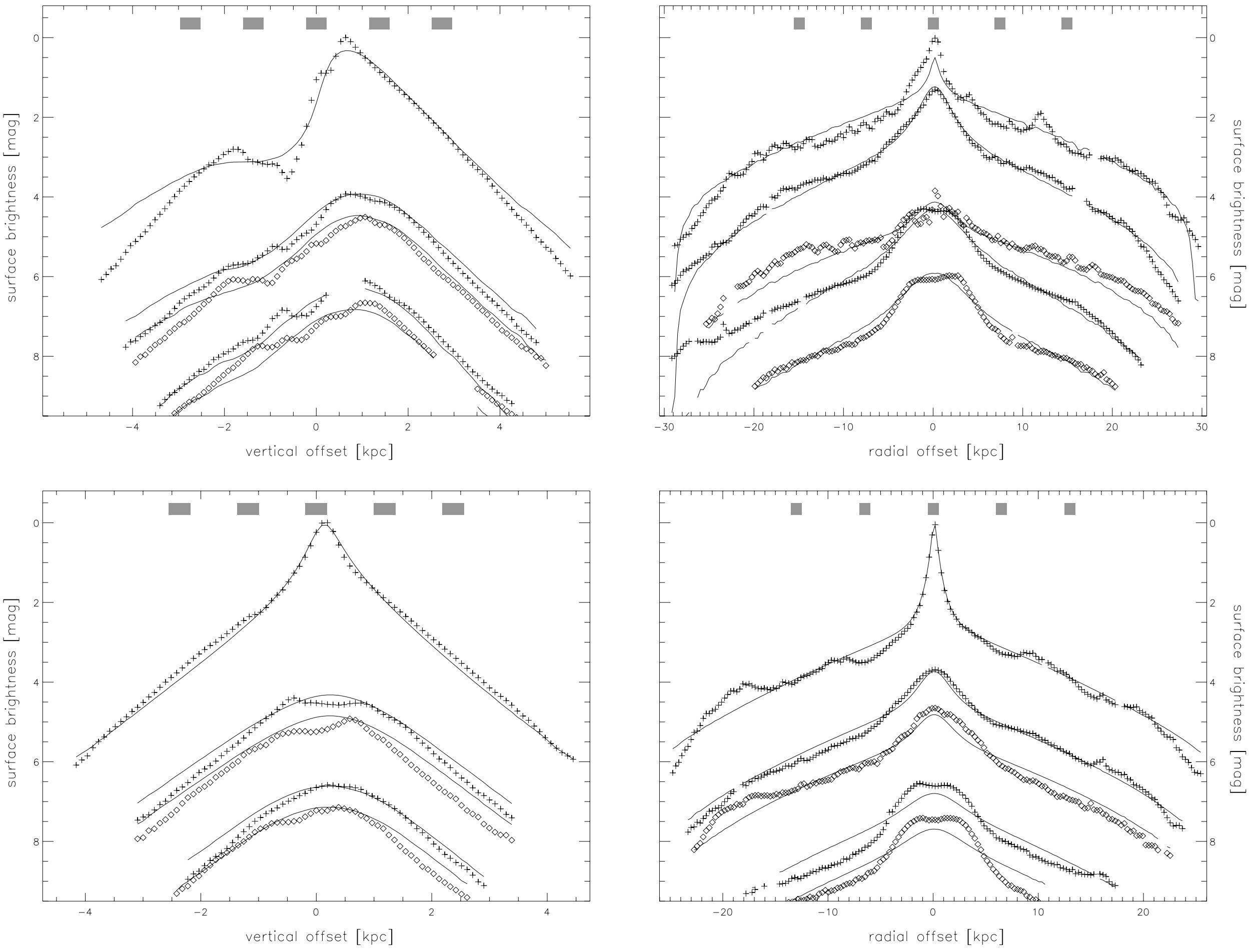

Fig. 14. Same as Fig. 4, but for NGC 5746.

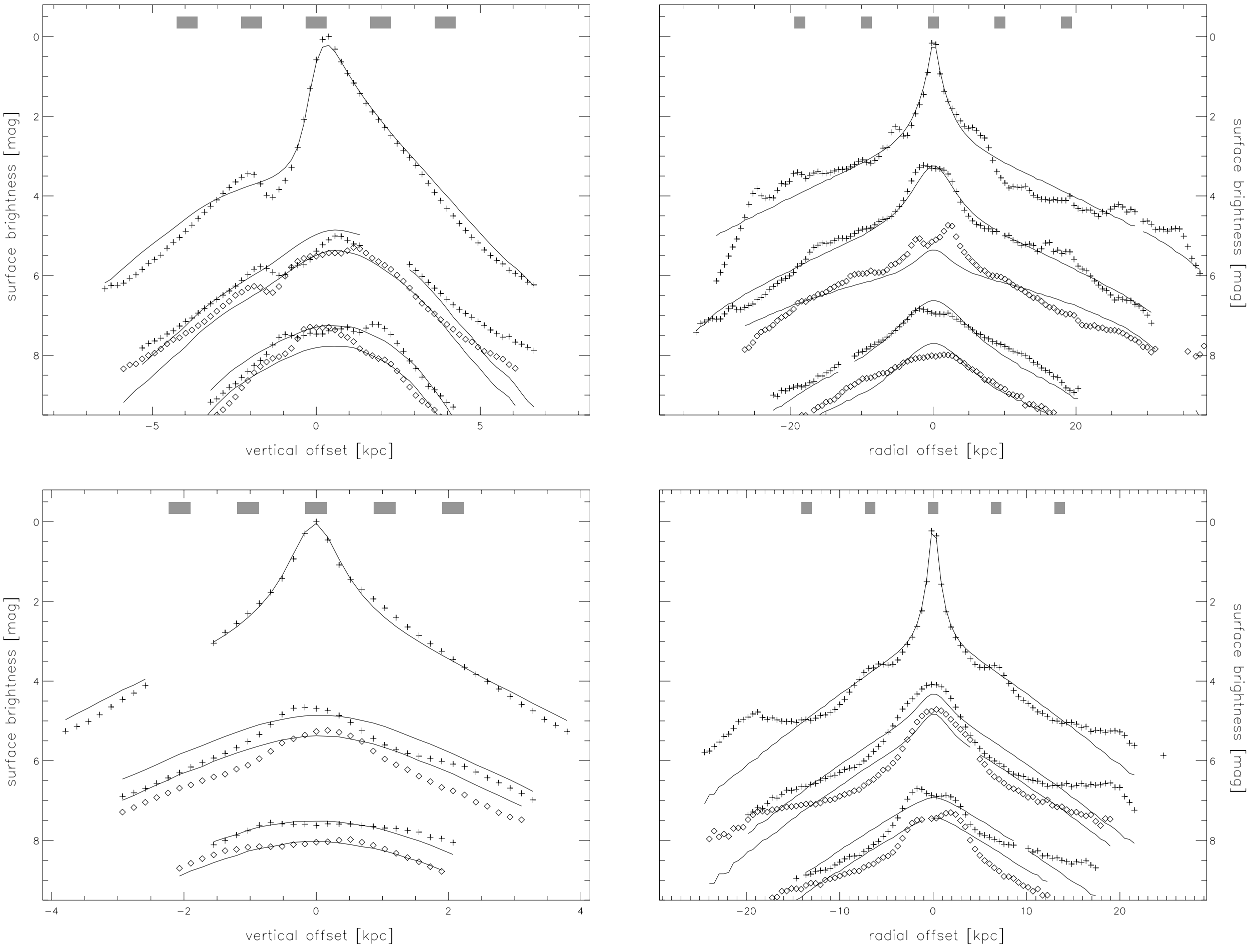

Fig. 15. Same as Fig. 4, but for NGC 5965.

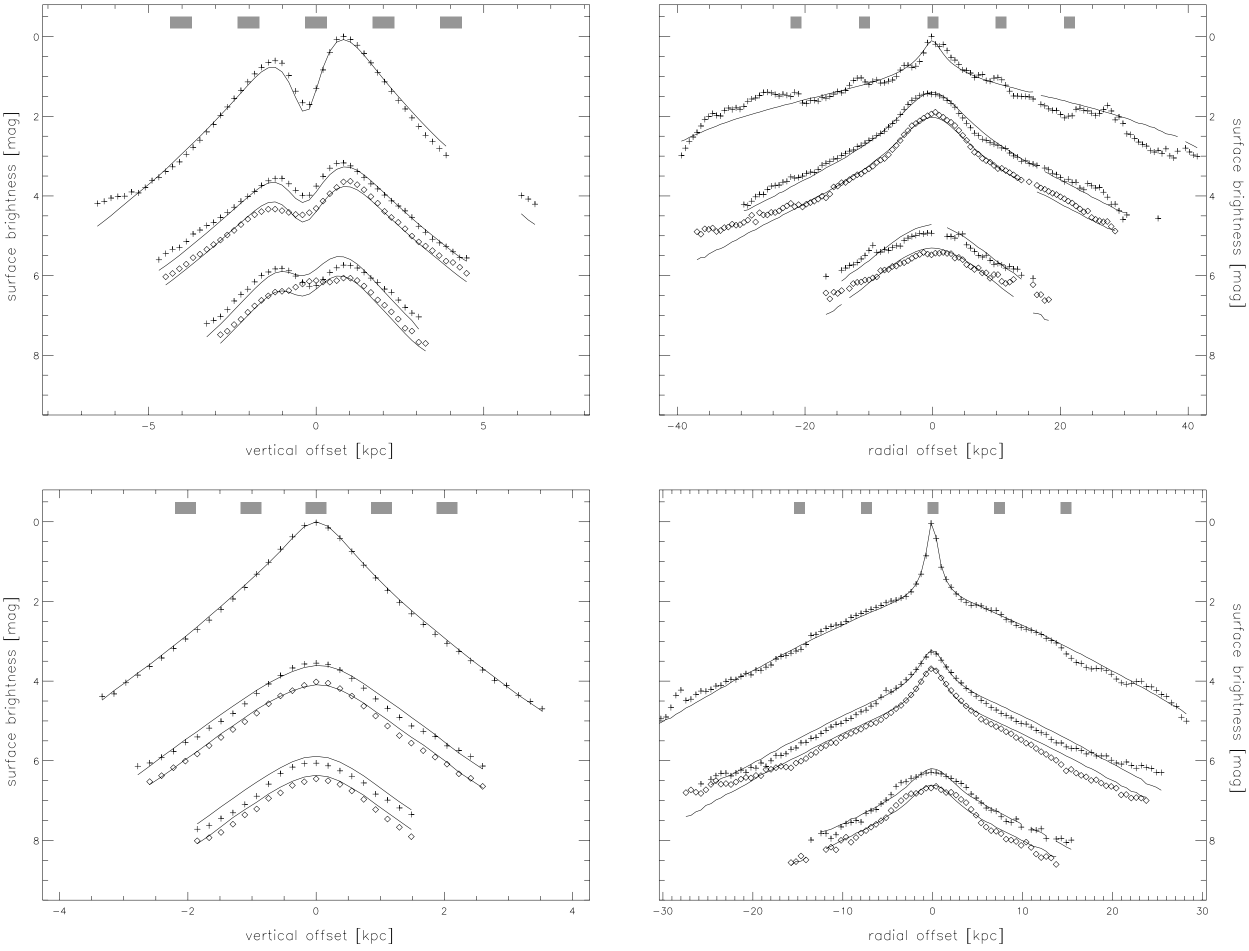

Fig. 16. Same as Fig. 4, but for UGC 4277.